Deconvoluting the impacts of the active material skeleton and the inactive phase morphology on the performance of lithium ion battery electrodes

Mehdi Chouchane, Alejandro A. Franco

Energy Storage Materials 47 (2022) 649–655

Contents lists available at ScienceDirect

Energy Storage Materials

journal homepage: www.elsevier.com/locate/ensm

Deconvoluting the impacts of the active material skeleton and the inactive phase morphology on the performance of lithium ion battery electrodes

Mehdi Chouchane [a,b], Alejandro A. Franco [a,b,c,d,*]

[a] Laboratoire de Réactivité et Chimie des Solides (LRCS), Université de Picardie Jules Verne, Hub de l'Energie, UMR CNRS 7314, 15 rue Baudelocque, 80039 Amiens Cedex, France
[b] Réseau sur le Stockage Electrochimique de l'Energie (RS2E), Hub de l'Energie, FR CNRS 3459, 15 rue Baudelocque, 80039 Amiens Cedex, France
[c] ALISTORE-European Research Institute, Hub de l'Energie, FR CNRS 3104, 15 rue Baudelocque, 80039 Amiens Cedex, France
[d] Institut Universitaire de France, 103 boulevard Saint Michel, Paris 75005, France

A B S T R A C T

In order to extract the most capacity out of Li-ion battery (LIB) active materials, the optimization of the electrodes architectures at the mesoscale is essential. This work focuses on the morphology of the inactive phase (carbon additives and binder) through a 3-D modeling approach based on stochastic generation of electrode mesostructures with realistic $LiNi_{1/3}Mn_{1/3}Co_{1/3}O_2$ particle size distributions. It was found that having the inactive phase as a film spread on the active material results in poorer performance in part due to the loss of active surface area when compared to an agglomerate-like morphology.

In the Lithium Ion Battery (LIB) field, 3-D computational modeling using continuum approaches supported on Finite Element or Volume Methods has known exciting new developments in the recent years. Whether it is the modeling of the dynamic mechanical stress during discharge [1], or the tremendous progress in the spatial resolution of imaging [2] that can later support simulations [3], 3-D modeling can assist in the optimization of the electrodes architectures. 3D-modeling can be also used to support the optimization of the electrodes manufacturing process through the simulation of the slurry , the drying [4] and the calendering [5,6].Furthermore, 3D-modeling can be used to support the optimization of the active material (AM) through its microstructure, size or surface [7,8], and of the inactive phase through its morphology and its part in the electrode formulation [9].

In the 3D-resolved computational models, the inactive phase (carbon additives and binder) is considered as a single phase as carbon and binder domains (CBD) in order to simplify the description of the electrode. In recent years, a growing interest has been observed on the understanding of how CBD impacts the electrode and/or cell performance. ,For instance, Danner *et al.* in late 2016 investigated the impact of a poorly connected CBD region on the performance of a thick cell [10]. Then, in 2019 an article published by us was addressing the physics that should be applied in a 3D-model to the CBD by comparing the impact of different hypotheses for the Li^+ transport through them, on the discharge performance of $LiNi_{1/3}Mn_{1/3}Co_{1/3}O_2$ (NMC111) electrodes [11]. More recently, Lu *et al.* reported a 3-D model where the microstructure of the CBD was explicitly resolved [3]. Furthermore, only Mistry *et al.* focused on the morphology of the inactive phase through a screening of different parameters to determine effective properties of stochastically generated 3-D structures and that were fed into a 1-D performance model [12]. Their approach allowed them to build 2-D classification graphs for the limitations of the system, but they used homogenized values for structural parameters and they could not capture the causal link at the particle level. It transpires that with the recent development of the field, it is necessary to investigate the influence of the CBD morphology on the electrodes performance based on 3D-resolved computational models.

To study the impact of the morphology of the CBD on the electrochemical behavior of an electrode, the systems studied in this work are half-cells with NMC111-based electrodes versus lithium, with a homogeneous separator, as it can be seen in Fig. S1 in the Supporting Information. The NMC111 electrodes are $40 \times 40 \times 60\ \mu m^3$ in order to have a large volume while keeping the computational cost at a reasonable level. This is a volume in the same order of magnitude of the ones typically arising from nano-computer tomography characterizations. The electrodes have a NMC:CBD weight ratio of 94:6, which is a composition relevant in battery industry. It is assumed that 50 % of the CBD is composed of micropores where the Li^+ can migrate but not intercalate at the interface with NMC [13]. The positive electrodes arose from stochastic generation, as illustrated in Fig. 1**a**, using an *in house* library of NMC particles obtained from tomography data to build the AM skeleton. Two different types of electrodes were generated: one with 33 % of porosity (25 % in the bulk and 8 % in the CBD micropores) called hereafter High Porosity -HP- electrode, and one with 25 % of porosity (15 % in the bulk and 10 % in the CBD micropores) called hereafter Low Porosity (LP) electrode. These two types of electrodes were generated twice for a total of four NMC skeletons (HP-1, HP-2, LP-1, LP-2)

* Corresponding author at: Laboratoire de Réactivité et Chimie des Solides (LRCS), Université de Picardie Jules Verne, Hub de l'Energie, UMR CNRS 7314, 15 rue Baudelocque, 80039 Amiens Cedex, France.
E-mail address: alejandro.franco@u-picardie.fr (A.A. Franco).

https://doi.org/10.1016/j.ensm.2022.02.016
Received 12 November 2021; Received in revised form 3 February 2022; Accepted 10 February 2022
Available online 12 February 2022

Abbreviations

AM	active material
CBD	carbon binder domains
DoD	depth of discharge
LIB	lithium-ion battery
NMC	$LiNi_{1/3}Mn_{1/3}Co_{1/3}O_2$
SoL	state of lithiation

to take into account the stochastic nature of the generation. Moreover, our INNOV algorithm that can control the morphology of the CBD was used to add the CBD as a film or as an aggregate [14]. For instance, for a given NMC skeleton HP-1, arose two electrodes with CBD as film ($HP\text{-}1_{film\text{-}1}$, $HP\text{-}1_{film\text{-}2}$) and two with CBD as aggregates ($HP\text{-}1_{agg\text{-}1}$, $HP\text{-}1_{agg\text{-}2}$). The difference between the two configurations can be seen in Fig. 1**(b,c)** for a slice of $HP\text{-}1_{film\text{-}1}$ and $HP\text{-}1_{agg\text{-}1}$ respectively. Finally, the electrode mesostructures were meshed using INNOV [14,15] (with all the NMC particles individually identified), and fed into a Newman-based [16,17] 3-D model developed in our previous studies [6,18], to simulate a galvanostatic discharge at a rate of 3C. The associated equations were solved in the software COMSOL Multiphysics®. The 3-D rendering of all the mesostructures generated as well as the particle size distribution of the four NMC skeletons generated are available, respectively in **Figs. S2** and **S3**, and the specific active surface area, the set of equations and parameters, respectively in **Tables S1–S3**.

In Fig. 2**a**, the discharge curves obtained for the four different cases are represented with the dispersion related to the stochastic nature of the electrode generation. For a given condition, for instance HP_{agg}, the results obtained with the electrode mesostructures with the same NMC skeleton (i.e. $HP\text{-}1_{agg\text{-}1}$ with $HP\text{-}1_{agg\text{-}2}$, and $HP\text{-}2_{agg\text{-}1}$ with $HP\text{-}2_{agg\text{-}2}$) have been averaged so the light green region is the area between the two discharge curves representing $HP\text{-}1_{agg}$ and $HP\text{-}2_{agg}$ mesostructures. In other words, the colored regions represent the impact of the NMC skele-

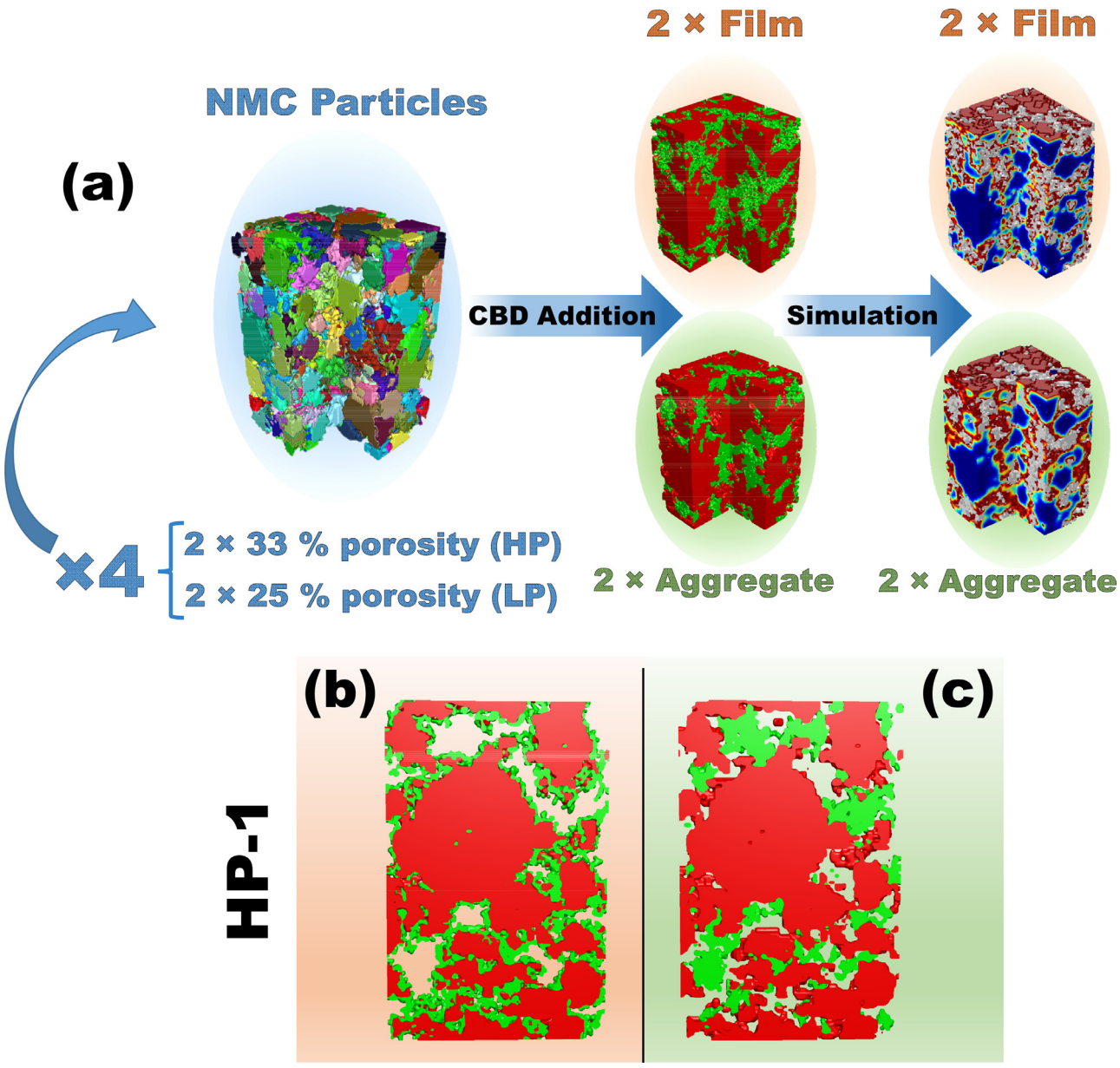

Fig. 1. (a) The workflow of the study with the generation of the four NMC particles structures, two with high porosity (HP) and two with low porosity (LP), followed by the stochastic addition of CBD twice as film and twice as aggregates and finally the 3-D electrochemical modeling. Slices of two electrodes with high porosity sharing the same NMC particles but different CBD morphologies: (b) the film one and (c) the aggregate one.

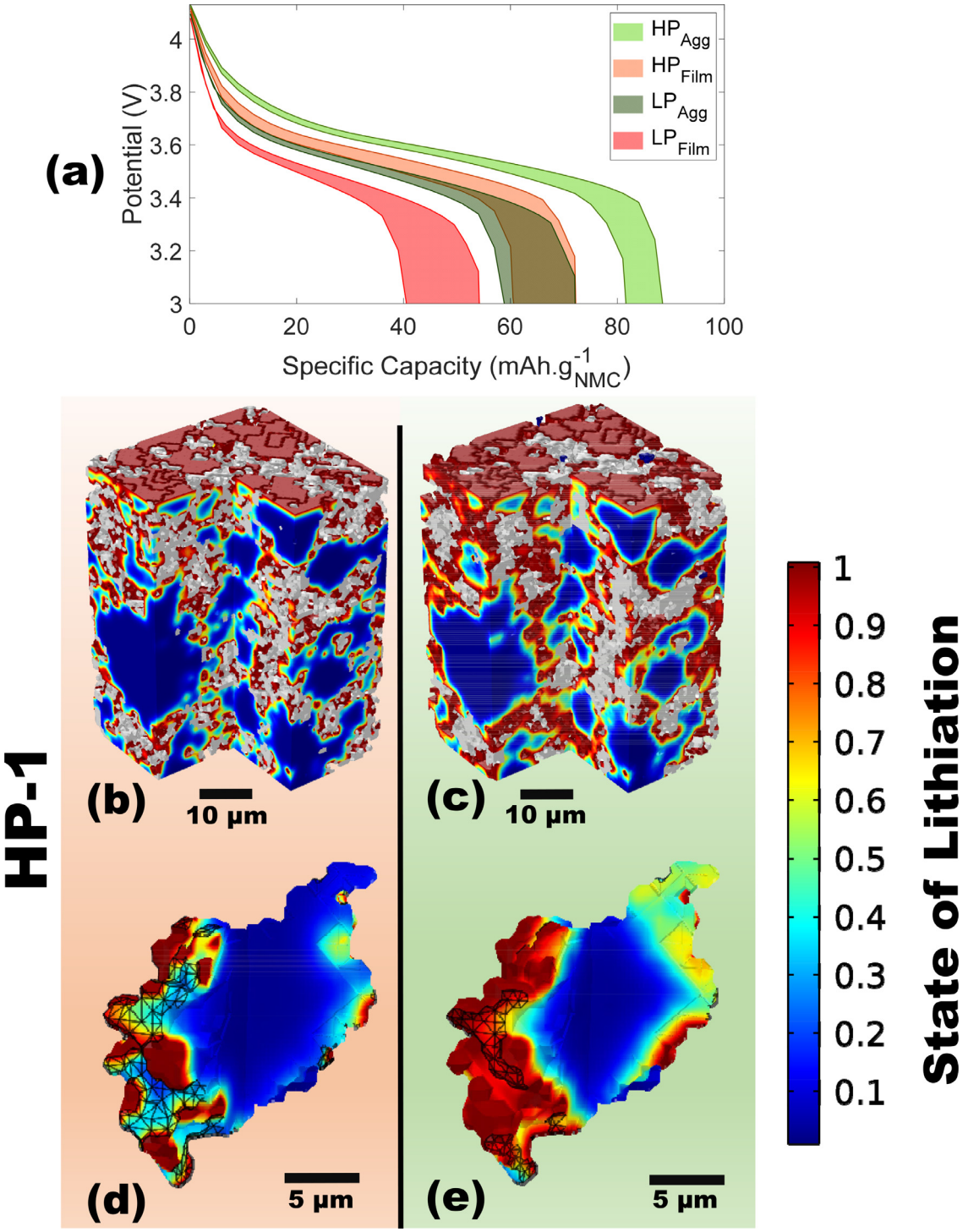

Fig. 2. (a) Discharge curves at a C-rate of 3C with the dispersion due to the NMC skeleton for each condition. The spatial distribution of the SoL at the end of discharge with the CBD in gray is reported for (b) HP-1$_{film-1}$ and (c) HP-1$_{agg-1}$, and also at the particle level with the surface of contact with CBD in black wireframe represented in (d) and (e).

ton on the behavior of the half-cell. It appears that differences from three distinct origins can be observed. Firstly, the impact of the CBD through the aggregates morphologies that perform better in terms of specific capacity with regards to the film configurations. Secondly, the significant variations due to the NMC skeleton are visible from the colored areas: for instance for the LP$_{film}$ case the specific capacities range from 41 to 54 mAh.g$^{-1}_{NMC}$. It is noteworthy that the dispersion due to the CBD addition (between HP-1$_{agg-1}$ and HP-1$_{agg-2}$ or LP-2$_{film-1}$ and LP-2$_{film-2}$ for instance) is almost negligible as illustrated in **Fig. S4**, which proves that more repetitions of the CBD addition step in the electrode stochastic generation are not necessary. Lastly, for the low porosity cases, for a given CBD morphology the specific capacities are systematically lower than the high porosity cases.

These macroscale discrepancies arose from lower scale differences, and in that regard 3-D computational modeling is a powerful tool to access observables (difficult to obtain experimentally) at any location

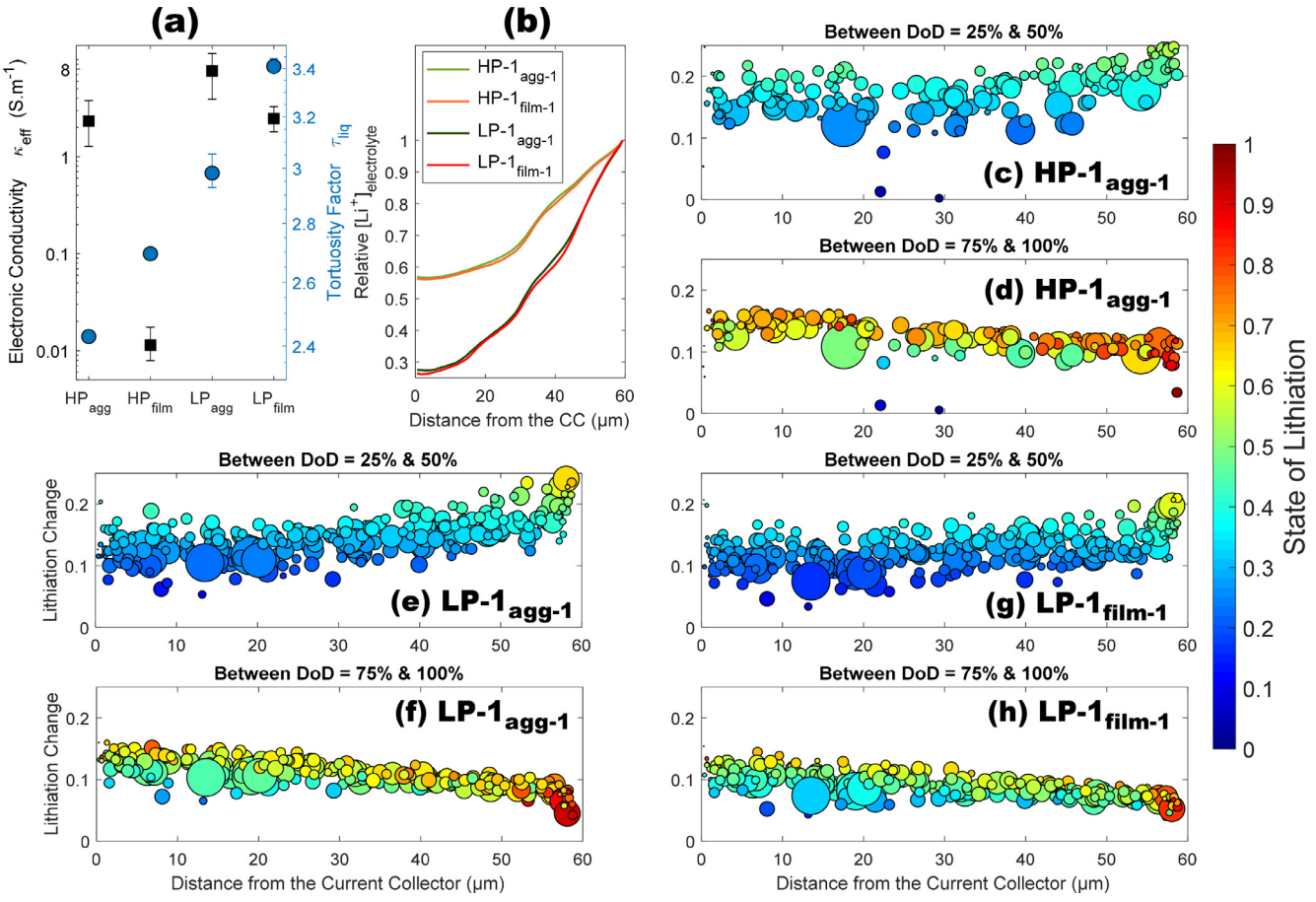

Fig. 3. (a) Effective electronic conductivities (■) and tortuosity factors (●) of the electrolyte (bulk + CBD micropores) averaged for the different conditions. (b) Normalized electrolyte concentration in Li^+ ($[Li^+]$ / $[Li^+]_{max}$) as a function of the distance from the current collector at the end of discharge for four conditions. (c–h) The lithiation change, *i.e.* the difference in lithiation state between two depths of discharge (DoD) as a function of the distance from the current collector. The color indicates the SoL of the particles at the intermediate DoD, *i.e.*37.5% and 87.5%, and the size of the disks is proportional to the volume of the NMC particles.

and time during the discharge process. The distribution of the state of lithiation (SoL), *i.e.* $[Li]_{NMC}$ /$[Li]_{NMC,max}$, is represented in Fig. 2**(b,c)** for HP-1 at the end of discharge for the film and aggregate-like CBD, respectively. Despite having the same NMC particles, the SoL is not distributed in the same manner at the electrode level. However, the solid diffusion is limiting in the two cases with the cores of the large NMC particles being almost unutilized during the discharge.

The impact of the CBD morphology also translates at the particle level by a heterogeneous distribution of the SoL as seen in Fig. 2**(d,e)**. For the film case (Fig. 2**d**), due to the loss of active surface area because of NMC/CBD contacts (represented by the black wireframe), the Li^+ will be intercalated at few "hotspots" leading to locally high SoL while for the CBD as aggregates (Fig. 2**e**), the distribution is more homogeneous because of the larger active surface area (surface area of contact with the electrolyte) available. Videos of the lithiation process happening at the electrode and particle scale for both CBD morphologies are available in the Supporting Information.

As seen previously, the lower porosity has a poorer rate capability than the higher porosity. Indeed, when the porosity is decreased, both the electronic conductivity and the tortuosity factor in the electrolyte will increase, the latter being detrimental to the performance of the battery cell. For a given AM and electrode composition, finding the optimal porosity is a trade-off between the ionic and electronic transport limitations. Here the effective electronic conductivity of the electrodes have been characterized using GeoDict® and the tortuosity factors in the electrolyte (taking into account the micropores in the CBD) have been determined thanks to TauFactor (Fig. 3**a**) [19].

The electrodes with CBD film-like morphology exhibit lower effective electronic conductivities than the electrodes with CBD-aggregate-like morphology. The difference is particularly significant for the high porosity electrodes, since the solid contact is improved as the porosity gets lower. This trend is not in agreement with the findings of Mistry et al. [12], who found that the film configuration had a higher effective electronic conductivity. This discrepancy can be explained by the difference in the algorithm used for the stochastic generation of CBD. Indeed, the present algorithm allows to have more pronounced differences at the electrode scale while the one used by Mistry et al. [12] has a higher impact at the microscale. In fact, the film configuration in Mistry et al. [12] results in a better-connected inactive phase when compared to the one in this work, which yields an improved effective conductivity of the film versus the aggregates in their case. While in our study, the CBD phase is more confined to the surface of the AM in the case of the film morphology, which hinders the connectivity of the inactive phase.

Moreover, the tortuosity factor τ_{liq} is higher for the LP electrodes (with CBD as film or as aggregate) and for the electrodes (HP or LP) with CBD as a film. Even though there is not experimental validation, one could postulate that due to the narrower space between NMC particles in the LP cases, the film configuration of the CBD results in a more systematic clogging of those pores. While, with a higher porosity, there are more pathways available for the Li^+ transport, and with CBD as aggregates, even though some pores might be fully clogged, large pores almost not clogged with CBD will remain to ensure a proper transport of Li^+. Yet, the difference of the profile of concentration of Li^+ at the end of discharge along the thickness of the electrode is almost negli-

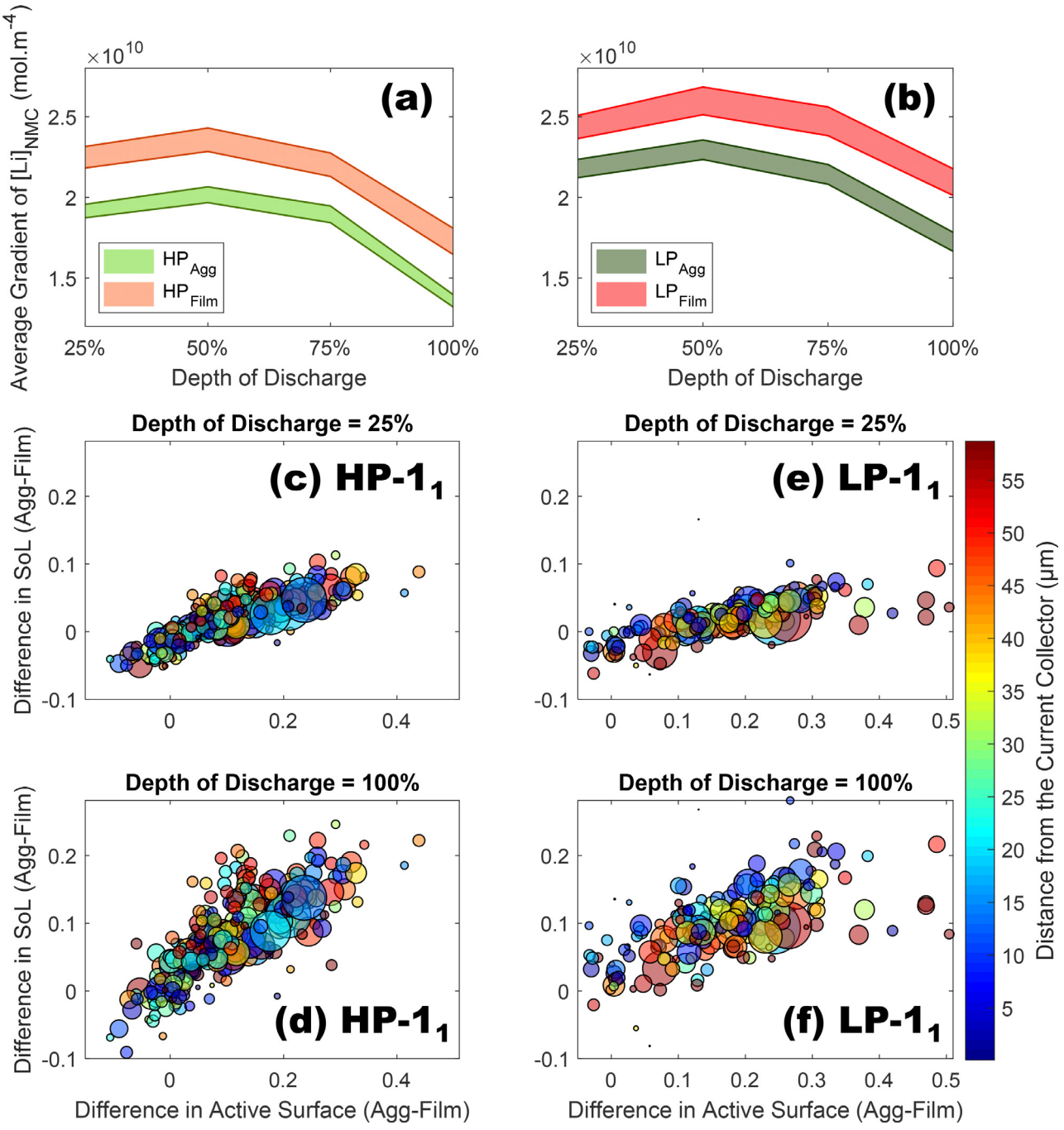

Fig. 4. The average gradient of Li in the NMC particles at different DoD for the (a) HP and (b) LP structures. (c–f) The difference in the state of lithiation versus the difference in relative active surface area (active surface area / (active surface area + NMC/CBD surface area)) for each of the particles in the electrode mesostructures with CBD as agglomerate and film.

gible between HP-1$_{agg}$ and HP-1$_{film}$, and between LP-1$_{agg}$ and LP-1$_{film}$ according to Fig. 3**b**. The gradient of concentration is driven by the NMC skeleton more than the CBD morphology, as LP-1 demonstrates a steeper gradient of concentration in the electrolyte than HP-1

From Fig. 3**(a,b)**, it comes that HP$_{agg}$ has a satisfactory effective electronic conductivity and a mild $[Li^+]_{electrolyte}$ gradient. The electrolyte ionic conductivity κ_{ion} is a function of the electrolyte concentration [20] as seen in **Fig. S5**, and in the range of values of $[Li^+]_{electrolyte}$, κ_{ion} is around 0.5 S.m^{-1}. For HP$_{agg}$, the effective electronic conductivity of the electrode κ_{eff} ranges from 1.27 S.m^{-1} to 3.78 S.m^{-1}, hence a dual limitation from the electronic and ionic transports. While for LP$_{agg}$, κ_{eff} and τ_{liq} are higher, hence a stronger ionic limitation (than the electronic one) visible from the gradient of $[Li^+]_{electrolyte}$ in Fig. 3**b**.

These observations will impact the lithiation process during the discharge, as illustrated by the lithiation change, *i.e.* the difference in SoL, between different depths of discharge (DoD) in Fig. 3**(c–h)**. This observable highlights how fast NMC particles are lithiated during a given period, here during the second and last quarters of the discharge. For HP-1$_{agg-1}$ in Fig. 3**(c,d)**, since both ionic and electronic limitations are not negligible, we do not obtain a clear trend where the top or bottom regions of the electrode are favored, instead the lithiation change is more or less homogeneous.

Now, if we take the example of an electrode with a more pronounced ionic transport limitation, *i.e.* LP-1_{agg-1}, it is clear from Fig. 3**e** that during the second quarter of discharge, the region closer to the separator is getting lithiated faster than the rest of the electrode, regardless of the size of the particles. The NMC particles in this region will reach a concentration close to the maximum one, entailing a decay of the lithiation speed in the last quarter of discharge as evidenced in Fig. 3**f**. Interestingly, LP-$1_{film-1,}$ that has the same NMC skeleton as LP-1_{agg-1}, hence a similar $[Li^+]_{electrolyte}$ gradient, demonstrates a milder gradient of lithiation change (Fig. 3**(g,h)**). The lithiation process is more homogeneous because the film configuration results in a lower κ_{eff} (2.03 $S.m^{-1}$ vs 7.08 $S.m^{-1}$), entailing a higher electronic limitation that will compete with the ionic transport limitation.

As highlighted in Fig. 2**(b–e)**, the CBD will not only impact in the electronic percolation, but also through the loss of active surface area where the Li^+ can react. Due to the limited surface area in the film cases, the appearance of "hotspots" for the lithiation of the NMC was demonstrated at the particle level. The resulting higher heterogeneity is also noticeable at the electrode level with the average $[Li]_{NMC}$ gradient reported as a function of the DoD in Fig. 4**(a,b)**. At first the gradient is increasing until DoD = 50% because the simulations start from a fully delithiated NMC, so the lithiation of the surface of the particles will drastically increase the gradient of concentration. Then, the average gradient drops thanks to the solid diffusion softening the intra-particles gradient and to the lithiation process happening at places less favorable because of the higher SoL of the more favorable active surface regions. The average gradients for the LP cases (Fig. 4**b**) are systematically higher for a given CBD morphology than the HP ones (Fig. 4**a**) because of a poorer electrode utilization in the LP cases as illustrated by the lower specific capacity in discharge (Fig. 2**a**). In their study, Mistry et al. [12] had also identified the loss of active surface area as one of the main factor to the drop of capacity in the electrode with CBD as film.

To go further in the analysis, it is possible with this computational tool, for a given NMC skeleton, to compare between NMC particles for electrodes with CBD as film or as aggregates. The difference in SoL as a function of the difference in relative surface area (active surface area / (active surface area + NMC/CBD surface area)) is represented for HP-1_{agg-1} - HP-1_{film-1} in Fig. 4**(c,d)**, and in Fig. 4**(e,f)** for LP-1_{agg-1} - LP-1_{film-1}. In both cases, there is a clear relationship between the difference in SoL and the difference in active surface area, almost linear for DoD = 25% in Fig. 4**(c,e)**. The more active surface area is available, the higher will be the SoL of the particles. Moreover, this SoL difference increases during the discharge as seen in Fig. 4**(d,f)**, with the slope coefficient (based on a linear fitting) increasing in average by *ca.* 75% between DoD = 25% and DoD = 100% as reported in **Fig. S6**.

For the LP-1 (Fig. 4**f**), it is noteworthy that between DoD = 25% and DoD = 100%, most of the particles demonstrating the highest SoL difference for a given difference in active surface area are located close to the current collector, while it was not the case for DoD = 25% (Fig. 4**e**). This can be explained by the higher lithiation change this region will undergo at the end of discharge due to ionic limitation as demonstrated in Fig. 3**(e–h)**.

This investigation allowed deconvoluting the influence of the NMC skeleton from the impact of the CBD morphology on the electrochemical behavior of the corresponding electrode. While the NMC skeleton has a higher impact on the electrolyte concentration gradient, at high porosities the CBD morphology will drive the effective electronic conductivity of the electrode. Furthermore, the CBD morphology will play a significant role on the lithiation process that will be more homogeneous in the case of an aggregate-like configuration because of the larger AM active surface area for the Li^+ to react. A heterogeneous lithiation process entails a higher utilization of given regions of the electrode, thus a risk of cracking due to the stress from the deep variations in SoL. It results that having control at the experimental level over the CBD morphology would be highly beneficial to the performance of a LIB cell, and this is a subject not so much addressed in the experimental literature.

Declaration of Competing Interest

No conflict of interest exists. We wish to confirm that there are no known conflicts of interest associated with this publication and there has been no significant financial support for this work that could have influenced its outcome.

CRediT authorship contribution statement

Mehdi Chouchane: Conceptualization, Methodology, Software, Formal analysis, Validation, Writing – original draft, Writing – review & editing, Visualization, Investigation. **Alejandro A. Franco:** Conceptualization, Methodology, Supervision, Funding acquisition, Writing – review & editing.

Acknowledgment

The authors acknowledge the European Union's Horizon 2020 research and innovation program for the funding support through the European Research Council (grant agreement 772873, "ARTISTIC" project). The authors acknowledge Dr. Oier Arcelus for the labeling of the NMC particles that were used for the stochastic generation. The authors acknowledge Jean-Baptiste Hoock and Laurent Renault for managing the MATRICS server at the Université de Picardie Jules Verne on which the simulations were performed. Punctual technical assistance of Chaoyue Liu, PhD student in the ARTISTIC project, is also highly appreciated. A.A.F. acknowledges the Institut Universitaire de France for the support.

Supplementary materials

Supplementary material associated with this article can be found, in the online version, at doi:10.1016/j.ensm.2022.02.016.

References

[1] M.E. Ferraro, B.L. Trembacki, V.E. Brunini, D.R. Noble, S.A. Roberts, Electrode mesoscale as a collection of particles: coupled electrochemical and mechanical analysis of NMC cathodes, J. Electrochem. Soc. 167 (1) (2020) 013543, doi:10.1149/1945-7111/ab632b.

[2] S.R. Daemi, C. Tan, T. Volkenandt, S.J. Cooper, A. Palacios-Padros, J. Cookson, D.J.L. Brett, P.R. Shearing, Visualizing the carbon binder phase of battery electrodes in three dimensions, ACS Appl. Energy Mater. 1 (2018) acsaem.8b00501, doi:10.1021/acsaem.8b00501.

[3] X. Lu, A. Bertei, D.P. Finegan, C. Tan, S.R. Daemi, J.S. Weaving, K.B.O. Regan, T.M.M. Heenan, G. Hinds, E. Kendrick, D.J.L. Brett, P.R. Shearing, 3D microstructure design of lithium-ion battery electrodes assisted by X-ray nano-computed tomography and modelling, Nat. Commun. 11 (2079) (2020) 1–13, doi:10.1038/s41467-020-15811-x.

[4] T. Lombardo, A.C. Ngandjong, A. Belhcen, A.A. Franco, Carbon-binder migration: a three-dimensional drying model for lithium-ion battery electrodes, Energy Storage Mater. 43 (2021) 337–347, doi:10.1016/j.ensm.2021.09.015.

[5] X. Lu, S.R. Daemi, A. Bertei, M.D.R. Kok, K.B. O'Regan, L. Rasha, J. Park, G. Hinds, E. Kendrick, D.J.L. Brett, P.R. Shearing, Microstructural evolution of battery electrodes during calendering, Joule 4 (12) (2020) 2746–2768, doi:10.1016/j.joule.2020.10.010.

[6] A.C. Ngandjong, T. Lombardo, E.N. Primo, M. Chouchane, A. Shodiev, O. Arcelus, A.A. Franco, Investigating electrode calendering and its impact on electrochemical performance by means of a new discrete element method model: towards a digital twin of Li-ion battery manufacturing, J. Power Sources 485 (2021) 229320, doi:10.1016/j.jpowsour.2020.229320.

[7] X. Lu, X. Zhang, C. Tan, T.M.M. Heenan, M. Lagnoni, K. O'Regan, S. Daemi, A. Bertei, H.G. Jones, G. Hinds, J. Park, E. Kendrick, D.J.L. Brett, P.R. Shearing, Multi-length scale microstructural design of lithium-ion battery electrodes for improved discharge rate performance, Energy Environ. Sci. (2021) 10.1039.D1EE01388B, doi:10.1039/D1EE01388B.

[8] G.J. Nelson, L.J. Ausderau, S. Shin, J.R. Buckley, A. Mistry, P.P. Mukherjee, V. De Andrade, Transport-geometry interactions in Li-ion cathode materials imaged using X-ray nanotomography, J. Electrochem. Soc. 164 (7) (2017) A1412–A1424, doi:10.1149/2.0261707jes.

[9] A.N. Mistry, P.P. Mukherjee, Probing spatial coupling of resistive modes in porous intercalation electrodes through impedance spectroscopy, Phys. Chem. Chem. Phys. 21 (7) (2019) 3805–3813, doi:10.1039/C8CP05109G.

[10] T. Danner, M. Singh, S. Hein, J. Kaiser, H. Hahn, A. Latz, Thick electrodes for Li-ion batteries: a model based analysis, J. Power Sources 334 (2016) 191–201, doi:10.1016/j.jpowsour.2016.09.143.

[11] M. Chouchane, A. Rucci, T. Lombardo, A.C. Ngandjong, A.A. Franco, Lithium ion battery electrodes predicted from manufacturing simulations: assessing the impact of the carbon-binder spatial location on the electrochemical performance, J. Power Sources 444 (2019) 227285, doi:10.1016/j.jpowsour.2019.227285.
[12] A.N. Mistry, K. Smith, P.P. Mukherjee, Secondary-phase stochastics in lithium-ion battery electrodes, ACS Appl. Mater. Interfaces 10 (7) (2018) 6317–6326, doi:10.1021/acsami.7b17771.
[13] L. Zielke, T. Hutzenlaub, D.R. Wheeler, C.W. Chao, I. Manke, A. Hilger, N. Paust, R. Zengerle, S. Thiele, Three-phase multiscale modeling of a $LiCoO_2$ cathode: combining the advantages of FIB-SEM imaging and X-ray tomography, Adv. Energy Mater. 5 (5) (2015) 1–8, doi:10.1002/aenm.201401612.
[14] M. Chouchane, A.A. Franco, An invitation to engage with computational modeling: user-friendly tool for in silico battery component generation and meshing, Batter. Supercaps 4 (2021) 1451–1456, doi:10.1002/batt.202100096.
[15] M. Chouchane, A. Rucci, A.A. Franco, A versatile and efficient voxelization-based meshing algorithm of multiple phases, ACS Omega 4 (6) (2019) 11141–11144, doi:10.1021/acsomega.9b01279.
[16] M. Doyle, T.F. Fuller, J. Newman, Modeling of galvanostatic charge and discharge of the lithium/polymer/insertion cell, J. Electrochem. Soc. 140 (6) (1993) 1526, doi:10.1149/1.2221597.
[17] M. Doyle, J. Newman, A.S. Gozdz, C.N. Schmutz, J. Tarascon, Comparison of modeling predictions with experimental data from plastic lithium ion cells, J. Electrochem. Soc. 143 (6) (1996) 1890, doi:10.1149/1.1836921.
[18] M. Chouchane, E.N. Primo, A.A. Franco, Mesoscale effects in the extraction of the solid-state lithium diffusion coefficient values of battery active materials: physical insights from 3D modeling, J. Phys. Chem. Lett. 11 (7) (2020) 2775–2780, doi:10.1021/acs.jpclett.0c00517.
[19] S.J. Cooper, A. Bertei, P.R. Shearing, J.A. Kilner, N.P. Brandon, TauFactor: an open-source application for calculating tortuosity factors from tomographic data, SoftwareX 5 (2016) 203–210, doi:10.1016/j.softx.2016.09.002.
[20] K.A. Smith, C.D. Rahn, C.Y. Wang, Control oriented 1D electrochemical model of lithium ion battery, Energy Convers. Manag. 48 (9) (2007) 2565–2578, doi:10.1016/j.enconman.2007.03.015.